Thermal properties of TiNiSn and VFeSb half-Heusler thermoelectrics from synchrotron x-ray powder diffraction

Daniella A. Ferluccio, Blair F. Kennedy, Sonia A. Barczak, Srinivas R. Popuri, Claire Murray, Michaël Pollet, Jan-Willem G. Bos

Thermal properties of TiNiSn and VFeSb half-Heusler thermoelectrics from synchrotron x-ray powder diffraction

IOP Publishing J. Phys. Energy 3 (2021) 035001 https://doi.org/10.1088/2515-7655/abf41a

Journal of Physics: Energy

OPEN ACCESS

RECEIVED
22 December 2020

REVISED
11 March 2021

ACCEPTED FOR PUBLICATION
31 March 2021

PUBLISHED
27 April 2021

PAPER

Thermal properties of TiNiSn and VFeSb half-Heusler thermoelectrics from synchrotron x-ray powder diffraction

Daniella A Ferluccio[1], Blair F Kennedy[1], Sonia A Barczak[1], Srinivas R Popuri[1], Claire Murray[2], Michael Pollet[3,4] and Jan-Willem G Bos[1,*]

[1] Institute of Chemical Sciences and Centre for Advanced Energy Storage and Recovery, School of Engineering and Physical Sciences, Heriot-Watt University, Edinburgh EH14 4AS, United Kingdom
[2] Diamond Light Source, Rutherford Appleton Laboratory, Harwell Oxford, Didcot OX11 0QX, United Kingdom
[3] CNRS, ICMCB, UPR 9048, Bordeaux, Pessac F-33600, France
[4] University of Bordeaux, ICMCB, UPR 9048, Bordeaux, Pessac F-33600, France
* Author to whom any correspondence should be addressed.

E-mail: j.w.g.bos@hw.ac.uk

Keywords: half-Heusler, thermoelectric, thermal expansion, thermal conductivity, TiNiSn, VFeSb

Supplementary material for this article is available online

Abstract

Half-Heusler (HH) alloys are an important class of thermoelectric materials that combine promising performance with good engineering properties. This manuscript reports a variable temperature synchrotron x-ray diffraction study of several TiNiSn- and VFeSb-based HH alloys. A Debye model was found to capture the main trends in thermal expansion and atomic displacement parameters. The linear thermal expansion coefficient $\alpha(T)$ of the TiNiSn-based samples was found to be independent of alloying or presence of Cu interstitials with $\alpha_{av} = 10.1 \times 10^{-6}$ K^{-1} between 400 and 848 K. The $\alpha(T)$ of VFeSb and TiNiSn are well-matched, but NbFeSb has a reduced $\alpha_{av} = 8.9 \times 10^{-6}$ K^{-1}, caused by a stiffer lattice structure. This is confirmed by analysis of the Debye temperatures, which indicate significantly larger bond force constants for all atomic sites in NbFeSb. This work also reveals substantial amounts of Fe interstitials in VFeSb, whilst these are absent for NbFeSb. The Fe interstitials are linked to low thermal conductivities, but also reduce the bandgap and lower the onset of thermal bipolar transport.

1. Introduction

Thermoelectric generators (TEGs) use arrays of n- and p-type semiconductors to convert waste heat into electricity and are a renewable energy technology that improves fossil fuel utilisation [1]. The efficiency of TEGs is largely determined by the dimensionless figure-of-merit, ZT of the semiconductors used. This is given by $ZT = (S^2/\rho\kappa)T$, where S is the Seebeck coefficient, ρ the electrical resistivity and κ the total thermal conductivity, which is the sum of the lattice (κ_{lat}) and electronic thermal conductivities (κ_{el}), and T is the absolute temperature [1]. Successful device operation requires comparable ZT, in the n- and p-types, but also similar mechanical properties [1, 2]. In particular, the thermal expansion coefficients, $\alpha(T)$ need to be matched to prevent cracking on temperature cycling [2].

Half-Heusler (HH) alloys are a well-established class of thermoelectric materials that combine good performance in both n- and p-types, scalable processing, favourable thermal stability and mechanical properties [3–8]. The HH alloys have XYZ stoichiometry where Z represents a main group metal, either Sn, Sb or Bi, whilst X and Y are usually transition metals, selected to achieve an 18 valence electron count [9]. The crystal structure consists of a face centred cubic lattice of Z atoms with X in all octahedral sites, whilst the Y metals occupy half the tetrahedral sites in a checkerboard arrangement [9].

In terms of their thermoelectric properties, HH alloys are characterised by large power factors, $S^2/\rho \sim$ 5–6 mW m^{-1} K^{-2} at 800 K, but are limited by high $\kappa_{lat} \sim$ 10–20 W m^{-1} K^{-1} at 300 K for the stoichiometric parent materials [10–12]. The relatively large κ_{lat} compared to other state-of-the-art thermoelectrics is linked to high mean velocities of sound, $v_s =$ 3000–3500 m s^{-1} [13, 14], and the absence

of strong anharmonic bonding, which limits the strength of Umklapp phonon scattering [15–17]. The most widely used route to reduce κ_{lat} is point defect engineering (usually alloying on X and Z sites), with grain size reduction and phase segregation also exploited [3, 4, 8].

Historically, most attention has focused on n-type XNiSn and p-type XCoSb (X = Ti, Zr, Hf), which have been investigated since the 1990s, leading to $ZT > 1$ at 500 °C–700 °C [18–24]. However, the last decade has seen the discovery of a range of other good HH compositions, most prominently, p-type X'FeSb (X' = V, Nb, Ta) [12, 14, 25, 26] and ZrCoBi which support $ZT > 1$ [13], and n-type $X'_{0.8+x}CoSb$ compositions with intrinsic X-site vacancies [27–29]. The improvements in materials performance have led to an increasing number of studies focused on TEG development, which demonstrate promising power outputs and efficiencies [30–34].

The $\alpha(T)$ of the HH materials has been investigated using dilatometry and diffraction studies. For XNiSn a substantial body of literature exists (reviewed in [35]), which reveals similar $\alpha_{av} = 9.9(2) \times 10^{-6}$ K^{-1} and $\alpha_{av} = 10.6(2) \times 10^{-6}$ K^{-1} between 300 and 875 K for X = Ti and Zr, whilst X = Hf has a lower $\alpha_{av} = 8.8(1) \times 10^{-6}$ K^{-1}. Dilatometry data on NbFeSb yielded $\alpha_{av} = 9.0(2) \times 10^{-6}$ K^{-1} between 300 and 1073 K with no data available for VFeSb [36].

Amongst the HH alloys, TiNiSn and VFeSb, are unique because they support large concentrations of interstitial metals, leading to metal-rich XYM_yZ compositions. In case of TiNiSn, 8%–10% interstitial Ni or Cu can occupy the vacant tetrahedral site in the crystal structure, affording a promising route to manipulate κ_{lat} and electrical properties [37–45]. Both Ni and Cu strongly suppress κ_{lat}, but whilst Ni also reduces the electron mobility, this does not occur for interstitial Cu, providing an elegant route towards enhancement of ZT [46]. In the case of VFeSb, interstitial Fe and V/Fe disorder have long been considered to be present [47–50], but recent work suggests that in addition to Fe interstitials, significant concentrations of vacancies may occur on the V and Fe sites, leading to a highly disordered crystal structure [51].

Here, we report an investigation into the thermal properties of a range of $XNiCu_ySn$ (X = Ti or $Ti_{0.5}Zr_{0.25}Hf_{0.25}$; y = 0, 0.075 and 0.1) and X'FeSb (X' = V, $V_{0.8}Ti_{0.2}$ or $Nb_{0.8}Ti_{0.2}$) HH alloys using synchrotron x-ray powder diffraction (SXRD). These compositions were chosen to assess the impact of interstitial Cu and X-site alloying in TiNiSn, and p-type doping using Ti in X'FeSb. Rietveld analysis was used to extract the lattice and atomic displacement parameters. These were simultaneously fitted to a Debye model enabling accurate determination of $\alpha(T)$ and vibrational properties of all atomic sites. The $\alpha(T)$ of the $XNiCu_ySn$ samples are similar and well-matched to the VFeSb-based HH alloys. However, $Nb_{0.8}Ti_{0.2}FeSb$ has a ~15% lower $\alpha(T)$, caused by a higher average bond strength. Debye temperatures ($\theta_{D,i}$) were extracted for all atomic sites (i) and reveal systematic trends consistent with changes in atomic mass and bond force constant. We also present thermoelectric property data for the X'FeSb samples, revealing a low $\kappa(T)$ for the X' = V and $V_{0.8}Ti_{0.2}$ samples, which is linked to the presence of Fe interstitials. $Nb_{0.8}Ti_{0.2}FeSb$, which contains no interstitial Fe, has a regular $\kappa(T)$, indicative of phonon transport limited by Umklapp and (X-site) point-defect scattering.

2. Experimental

The synthesis and thermoelectric properties of the TiNiSn, $TiNiCu_{0.1}Sn$ and $Ti_{0.5}Zr_{0.25}Hf_{0.25}NiCu_{0.075}Sn$ samples used in this study were reported previously [45, 46]. Polycrystalline VFeSb, $V_{0.8}Ti_{0.2}FeSb$ and $Nb_{0.8}Ti_{0.2}FeSb$ samples were prepared using a similar solid-state route. This involves intimate mixing of stoichiometric amounts of V (−325 mesh, 99.95%), Ti (−325 mesh, 99.999%), Sb (powdered shots, 99.85%), Nb (−325 mesh, 99.999%) (all Alfa Aesar) and Fe (powder, ⩾99%, Sigma Aldrich) using a mortar and pestle. The mixed powders were cold pressed into pellets and wrapped in Ta foil and heated at 800 °C or 900 °C (V, Nb compositions, respectively) for 24 h inside vacuum sealed quartz tubes. After homogenisation using mortar and pestle, the samples were cold pressed, wrapped in Ta foil and heated under the same conditions for a further ten days. Following synthesis, the samples were hot pressed at 800 °C or 900 °C (V, Nb compositions) and 80 MPa applied pressure inside graphite dies using a homebuilt hot press. The densities of the hot-pressed pellets were 93(1)% of the theoretical x-ray density. S and ρ were measured using a Linseis LSR-3 instrument on bar-shaped specimens cut from the hot-pressed disks. The thermal diffusivity (D) was measured on hot pressed cylindrical disks using a Linseis LFA instrument. The thermal conductivity $\kappa = DC_pd$ was calculated by multiplication with the gravimetric density (d) and heat capacity (C_p) obtained from the literature [12]. A Maxwell–Eucken porosity correction was applied to the measured κ [29].

SXRD data was collected on the I11 beamline at Diamond Light Source, Oxford, UK using five MAC arms with a total of 45 individual analyser-detector channels [52]. The synchrotron wavelength was 0.49397(1) Å. Heating and cooling was carried out using a Cyberstar hot air blower, with the measurements carried out in the 300 K–848 K temperature range, using a heating rate of 10 °C min^{-1}, with data collected every 30 °C, with a collection time of 2 s/scan. A Pt standard was used as a temperature reference, calculation

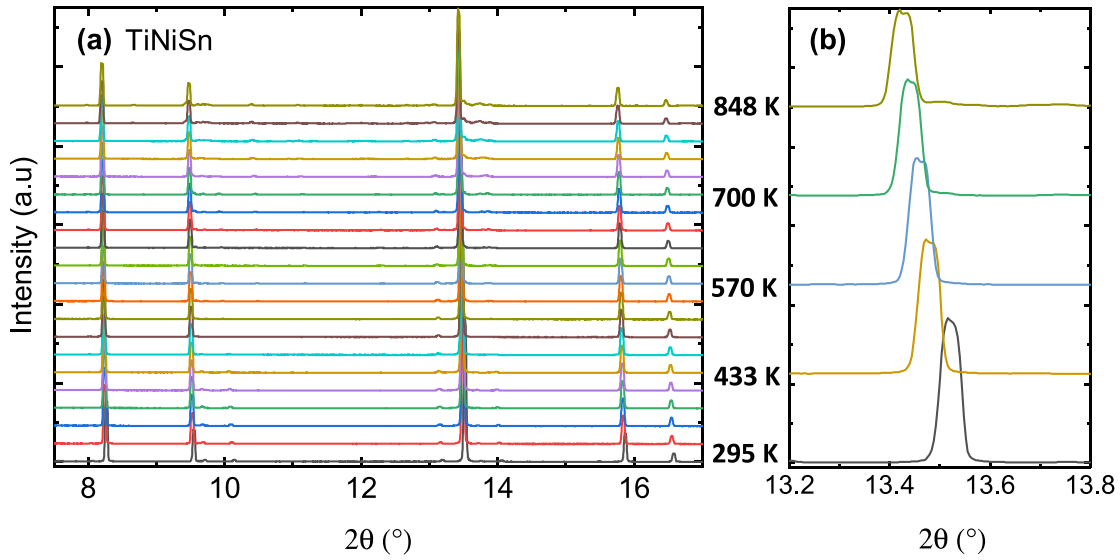

Figure 1. Variable temperature synchrotron x-ray powder diffraction patterns for TiNiSn. Panel (a) illustrates the lattice expansion and phase stability. Panel (b) confirms the absence of significant peak broadening on heating. Datasets are used as collected and have been offset with respect to each other.

of the actual temperatures was derived from the refined lattice parameters and literature [53]. Prior to data collection, all samples were finely ground using mortar and pestle and loaded into thin-walled 0.1 mm diameter quartz capillaries to minimise x-ray absorption. All data underwent Rietveld refinement using the GSAS software [54] and EXPGUI interface [55]. Corrections were made for anomalous scattering and x-ray absorption using the XPrime programme.

3. Results

3.1. HH compositions

Variable temperature SXRD patterns for TiNiSn collected between 295 and 848 K are shown in figure 1, whilst equivalent plots for the other compositions can be found in figures S1–S5 (available online at stacks.iop.org/JPENERGY/3/035001/mmedia) in the supplemental information. Inspection after cooling revealed that for all samples, except for $Ti_{0.5}Zr_{0.25}HfNiCu_ySn$, the thin-walled capillaries had broken, leading to exposure of the fine powders to air. Despite this, all samples show good stability up to 848 K with the dominant peaks originating from the HH phase. An overview of the fitted unit cell and atomic parameters and fit statistics at 295 K, 570 K and 848 K is given in tables S1 and S2 in the SI.

The 295 K data were used to determine the experimental compositions of the HH phases. For the $XNiCu_ySn$ samples, this confirmed the results of earlier neutron powder diffraction studies [45, 46]. TiNiSn forms with some excess Ni on the vacant tetrahedral site with a refined $TiNi_{1.036(3)}Sn$ composition. $TiNiCu_{0.10}Sn$ has an experimental composition of $TiNiCu_{0.087(5)}Sn$, in good agreement with the nominal composition, allowing for a small amount of Cu segregation during hot pressing [45]. The $Ti_{0.5}Zr_{0.25}Hf_{0.25}Cu_{0.075}Sn$ sample could be fitted using a single HH phase, despite the known tendency of Ti and Zr/Hf to phase segregate [46]. We have previously shown that the presence of Cu leads to improved mixing of the X-site elements, although traces of segregation remain at micron length scales [46]. The refined composition of this sample is $Ti_{0.54(1)}Zr_{0.23(1)}Hf_{0.23(1)}Cu_{0.052(4)}Sn$.

By comparison to XNiSn, there is far less detailed diffraction work on the X'FeSb HH alloys. In addition, X'FeSb samples in the literature are generally prepared using melt-based routes [25, 26, 56, 57], whereas we have exploited powder reactions. The VFeSb and doped $V_{0.8}Ti_{0.2}FeSb$ samples were difficult to prepare phase pure, unlike $Nb_{0.8}Ti_{0.2}FeSb$ (figures S1–S5). This situation is somewhat reminiscent of the difficulty in obtaining high quality TiNiSn compared to $Zr_{1-x}Hf_xNiSn$ [40]. The composition for VFeSb was refined to be $VFe_{1.064(2)}Sb$, while two HH phases were evident in the Ti substituted sample. Here, the main HH phase (90 wt%) has $V_{0.8}Ti_{0.2}Fe_{1.035(2)}Sb$ composition, while the minor phase (10 wt%) has a fitted $VFe_{1.068(2)}Sb$ composition, similar to the VFeSb sample. The observed lattice parameters correlate with the fitted amount of Fe on the interstitial site (table S2). Note that it is not possible to refine the V/Ti ratio due to their near identical x-ray scattering strength. By contrast, the fitted composition for $Nb_{0.8}Ti_{0.2}FeSb$ is $Nb_{0.80(1)}Ti_{0.20(1)}Fe_{1.000(5)}Sb$, and therefore reveals no evidence for Fe interstitials. We tested for the possibility

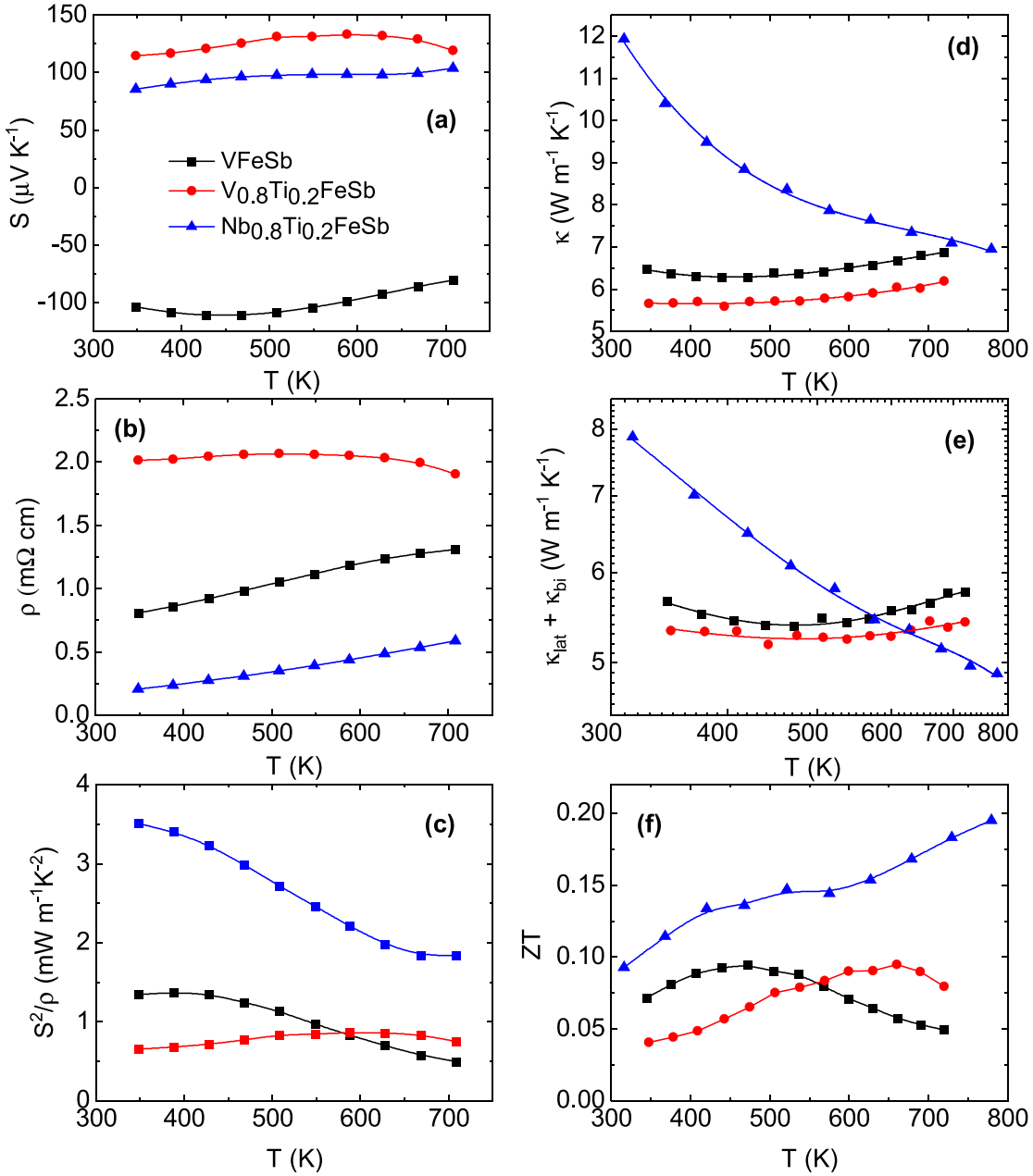

Figure 2. Temperature dependence of (a) the Seebeck coefficient (S), (b) the electrical resistivity (ρ), (c) the power factor (S^2/ρ), (d) the total thermal conductivity (κ), (e) the lattice and bipolar thermal conductivities ($\kappa_{lat} + \kappa_{bi}$) and (f) figure of merit (ZT) for the X'FeSb samples.

of vacancies on the V and Fe (Y1) sites in VFeSb, but this did not lead to improvements in the quality of the fit. The model with only interstitial Fe is therefore the simplest to describe the data and was used throughout. Trial fits to assess if the HH composition had changed on heating to 848 K showed no evidence for substantial variations and the 295 K compositions were used in all refinements. Furthermore, there is no evidence for significant peak broadening of the HH phase upon heating, neither from visual inspection nor from the refined profile parameters.

3.2. Thermoelectric properties

The measured $S(T)$, $\rho(T)$ and $\kappa(T)$ of the X'FeSb samples are shown in figure 2, together with the calculated power factor, S^2/ρ, sum of the lattice and bipolar thermal conductivity ($\kappa_{lat} + \kappa_{bi}$) and figure of merit, ZT. For completeness, the ZT values for the $XNiCu_ySn$ samples are $ZT = 0.35$ ($TiNiSn$), $ZT = 0.55$ ($TiNiCu_{0.1}Sn$) and $ZT = 0.5$ for ($Ti_{0.5}Zr_{0.25}Hf_{0.25}NiCu_{0.075}Sn$; all at 773 K) [45, 46]. The last two compositions correspond to the solubility limit of Cu, with optimal $ZT = 0.6/0.8$ observed at lower Cu content.

3.2.1. Electronic properties

The VFeSb sample shows n-type behaviour and has a metal-like $\rho(T)$, indicative of extrinsic doping (figures 2(a) and (b)), consistent with literature results [50, 51]. The $S(T)$ has a maximum at 450 K, signalling the onset of minority carrier (intrinsic) conduction. This is reflected in S^2/ρ, which is 1.4 mW m^{-1} K^{-2} at 400 K, gradually decreasing to 0.5 mW m^{-1} K^{-2} at 710 K (figure 2(c)). The general behaviour of S^2/ρ is similar to the literature [50, 51], but its magnitude is 2–3 times smaller due to a larger $\rho(T)$. The $V_{0.8}Ti_{0.2}FeSb$ sample has positive $S(T)$ values, confirming the successful substitution of Ti and p-type doping (figure 2(a)). The maximum in $S(T)$ is increased to 590 K, consistent with carrier doping. The onset of intrinsic conduction is also evident in $\rho(T)$ which has a downturn above ∼600 K. Both VFeSb samples therefore show significant intrinsic conduction above 450 K–590 K. This is consistent with the small bandgap, $E_g \sim 0.35$ eV, which is further reduced when interstitial Fe is present [51]. The p-type $Nb_{0.8}Ti_{0.2}FeSb$ sample has by far the best thermoelectric properties, due to much lower $\rho(T)$ values (figure 2(b)). This supports a promising $S^2/\rho = 3.5$ mW m^{-1} K^{-2} at 345 K, with the increasing ρ causing a reduction to $S^2/\rho = 1.8$ mW m^{-1} K^{-2} at 710 K (figure 2(c)). Compared to the literature, S^2/ρ at 345 K is similar (c.f. ∼4.5 mW m^{-1} K^{-2}) [12], but much lower at 710 K, where literature values ∼5.5 mW m^{-1} K^{-2} have been reported [12]. This discrepancy is caused by a reduced $S(T)$: our data saturates at +100 μV K^{-1} (figure 2(a)), whereas literature samples show linear increases (e.g. to +175 μV K^{-1} at 723 K) [12]. This difference cannot be attributed to thermal excitation across the bandgap as neither $\rho(T)$ nor $\kappa(T)$ shows evidence for intrinsic electronic transport.

3.2.2. Thermal transport

The $\kappa(T)$ and $\kappa_{lat}(T) + \kappa_{bi}(T)$ for the X'FeSb samples are shown in figures 2(d) and (e). Here, $\kappa_{lat} + \kappa_{bi}$ was calculated by subtracting the electronic thermal conductivity, $\kappa_{el} = LT/\rho$ from $\kappa(T)$. Here, L is the Lorenz number, which was obtained from $S(T)$ following [58]. The $\kappa_{lat} + \kappa_{bi}$ for the VFeSb samples is characterised by a shallow minimum at 450 K–550 K (figure 2(e)). Above this temperature, intrinsic conduction leads to a rapidly increasing $_{bi} = ATe^{-E_g/k_BT}$. Here A is a pre-factor, k_B is Boltzmann's constant and the Arrhenius term reflects the intrinsic electrical conduction [59]. The $\kappa_{lat} + \kappa_{bi}$ is near identical to published data on 'defective' VFeSb [51], but different from the $\sim T^{-n}$ dependence ($n \sim 0.7$) observed for 'defect-free' VFeSb [50]. The latter has κ_{lat} ∼11 W m^{-1} K^{-1} at 350 K [50], compared to much lower values ∼5.5 W m^{-1} K^{-1} for our samples and the 'defective' literature sample [51]. The κ_{lat} for $Nb_{0.8}Ti_{0.2}FeSb$ (figure 2(e)) is consistent with literature data [12] and has a fitted exponent, $n = 0.5$, consistent with point-defect phonon scattering [60]. (note that $n = 1$ signals Umklapp scattering dominated thermal transport and is indicative of a defect-free material). There is no evidence for a substantial κ_{bi}, which is consistent with the observed electrical transport. The overall conclusion is that whilst the Fe interstitials in VFeSb strongly reduce κ_{lat}, they also cause a reduction in E_g, leading to detrimental κ_{bi} at low temperatures. By contrast, the larger $E_g = 0.5$ eV [61], and the absence of Fe interstitials mean no intrinsic conduction and κ_{bi} are observed for NbFeSb.

3.2.3. Figure of merit

The $ZT(T)$ for the X'FeSb samples are shown in figure 2(f). VFeSb and $V_{0.8}Ti_{0.2}FeSb$ have comparable peak $ZT = 0.1$ at 470 K and at 660 K, with the increase in temperature reflecting the different onset of intrinsic conduction. This is about three times lower than literature ZT values [50, 51], which is attributable to the large $\rho(T)$ for our samples. The absence of bipolar transport means that $ZT(T)$ for $Nb_{0.8}Ti_{0.2}FeSb$ gradually increases to $ZT = 0.2$ at 773 K. This is lower than literature values ($ZT \sim 0.7$ at 773 K) [12], with the deficit caused by the lower $S(T)$ for our sample. Finally, we note that the thermal expansion and atomic parameters discussed in this manuscript are derived using Rietveld analysis of diffraction data and do not depend on control of the microstructure, which is vital in extracting high ZT values.

3.3. Variable temperature SXRD data

The temperature dependence of the lattice parameters (a) and thermal displacement parameters (U_{iso}) of the $XNiCu_ySn$ and X'FeSb samples are given in figures 3 and 4, respectively. These data were fitted simultaneously to a Debye model using the following expressions [62, 63]:

$$a(T) = a_0 + b\left[\int_0^T 9R\left(\frac{T}{\theta_D}\right)^3 dt \int_0^{\frac{\theta_D}{T}} \frac{x^4 e^x}{(e^x-1)^2} dx\right] \quad (1)$$

$$U_{iso,i}(T) = \frac{3h^2T}{m_i k_B \theta_{D,i}^2}\left[\frac{T}{\theta_{D,i}} \int_0^{\theta_{D,i}/T} \frac{x}{\exp(x)-1} dx + \frac{\theta_{D,i}}{4T}\right] + \sigma_i^2. \quad (2)$$

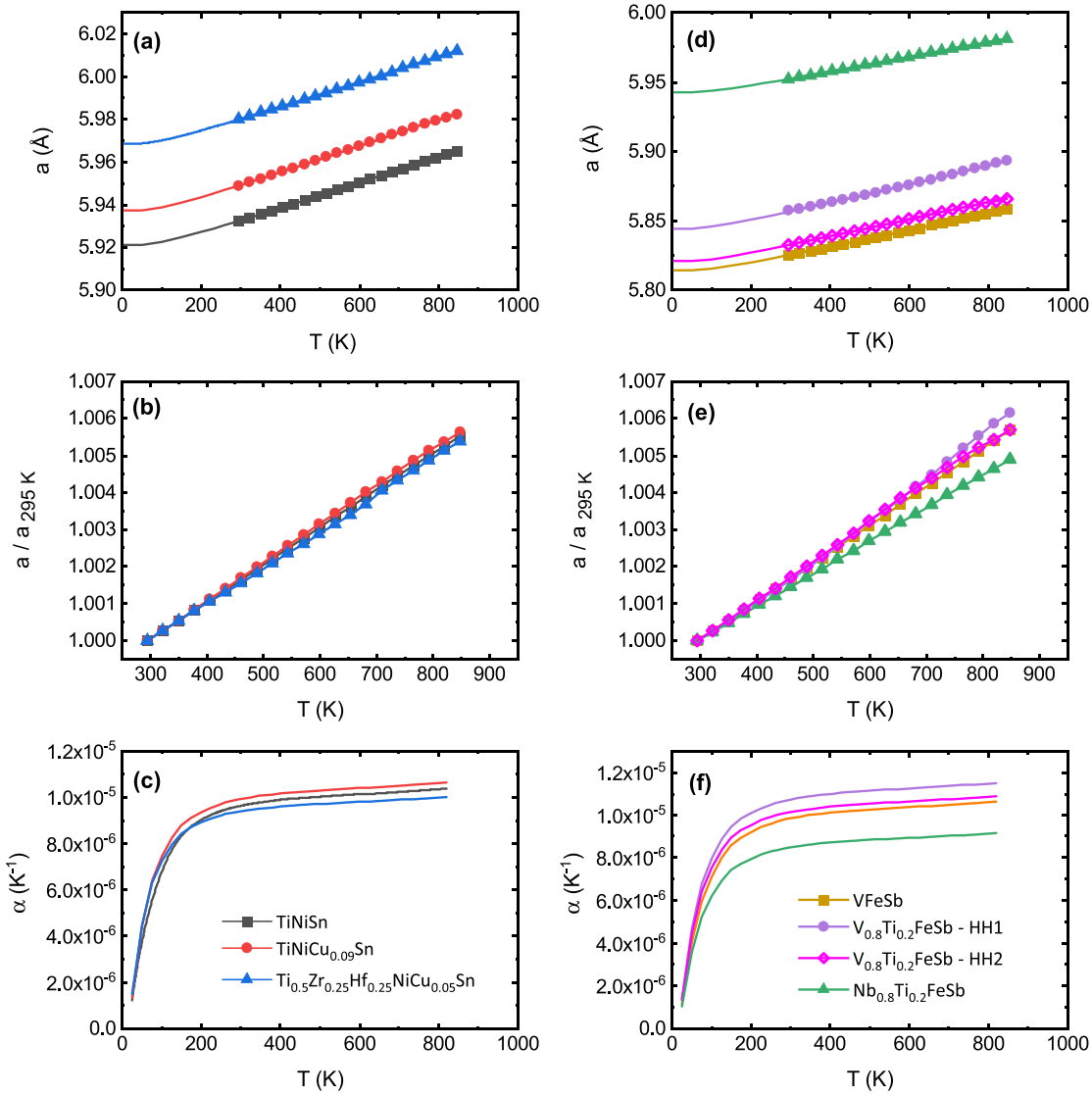

Figure 3. Temperature dependence of the lattice parameters (a), normalised lattice parameters (a/a_{295K}) and thermal expansion coefficients (α) for (a)–(c) the XNiSn and (d)–(f) the X'FeSb samples. The solid lines through $a(T)$ are the Debye fit as described in the text.

Here a_0 is the lattice parameter at 0 K, b is a scaling constant, R is the ideal gas constant, θ_D (θ_{Di}) is the average (atomic site) Debye temperature, h is Plank's constant, m_i is the Debye oscillator mass, k_B is Boltzmann's constant and σ_i^2 is the displacement correlation function. The index (i) refers to the individual crystallographic sites (X, Y or Z positions) or to the average of the sites. In these fits, the average U_{iso} and $a(T)$ were fitted simultaneously. A summary of the obtained θ_D, σ^2, a_0 and b values is given in table 1. High-temperature U_{iso} fitting has been widely applied to thermoelectric materials and is found to yield reliable estimates of the Debye temperature [64]. The simultaneous fitting of the lattice parameter is less common but improves the accuracy of the result. The thermal expansion was calculated from $a(T)$ using:

$$\alpha(T) = \frac{1}{a(T)}\frac{\mathrm{d}a(T)}{\mathrm{d}T}. \tag{3}$$

3.3.1. Thermal expansion

The $a(T)$ of the $XNiCu_ySn$ samples have a similar appearance with only minor differences in magnitude (figure 3(a)). This near identical behaviour is confirmed by the normalised lattice parameters ($a/a_{295\,K}$) and $\alpha(T)$ in figures 3(b) and (c) that nearly coincide. The lattice expands by ~0.6% upon heating to 848 K with an average $\alpha_{av} = 10.1(3) \times 10^{-6}\ K^{-1}$ for all samples between 400 K and 848 K (table 1). These values are in near perfect agreement with published α_{av} values for the XNiSn system [35].

By contrast, the X'FeSb samples show more divergent behaviour with $a/a_{295\,K}$ increasing by ~0.6% for the VFeSb-based samples, while $Nb_{0.8}Ti_{0.2}FeSb$ expands by only ~0.5% up to 848 K (figure 3(e)). This

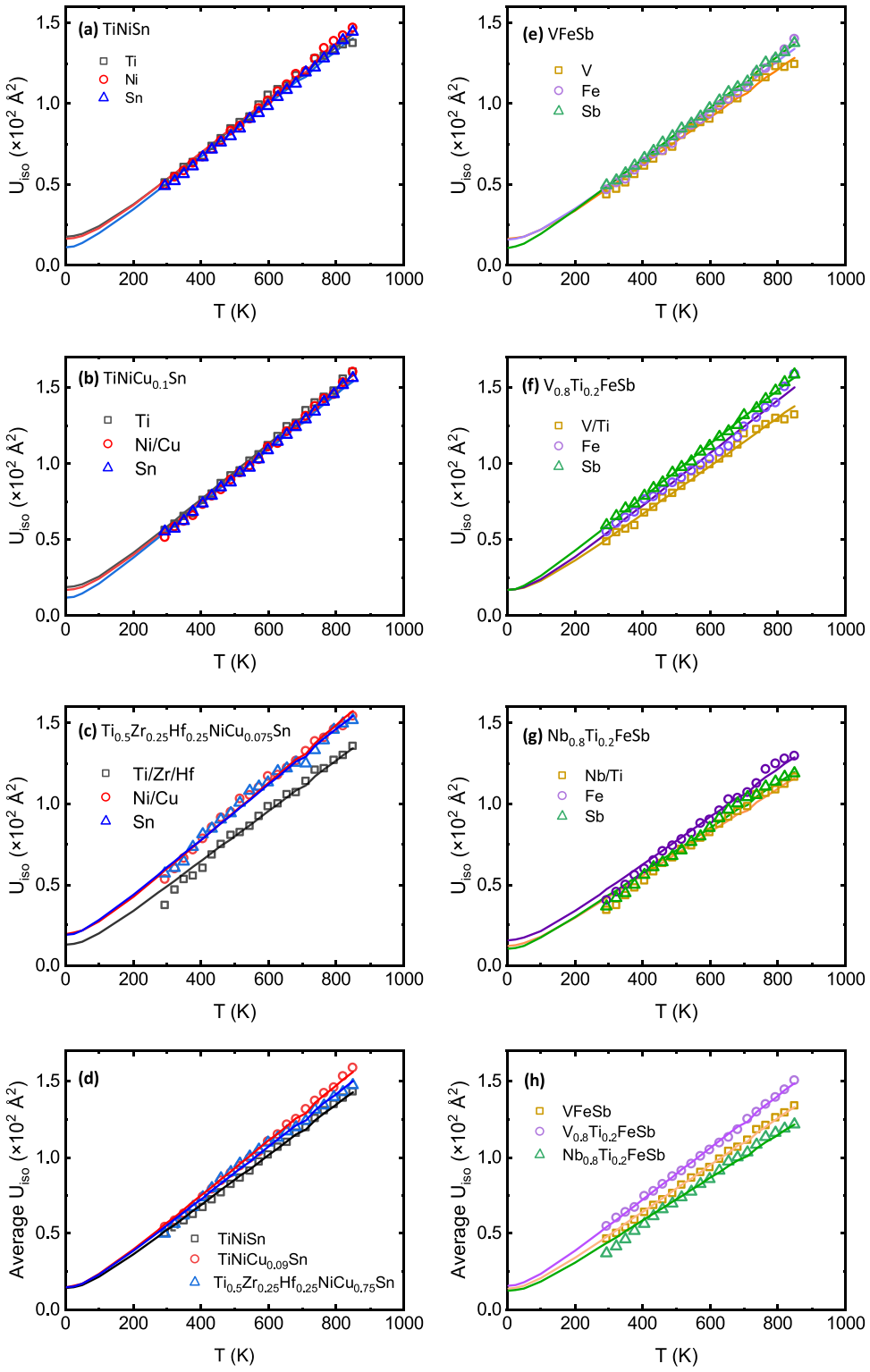

Figure 4. Temperature dependence of the atomic displacement parameters (U_{iso}) for (a) TiNiSn, (b) $TiNiCu_{0.1}Sn$, (c) $Ti_{0.5}Zr_{0.25}Hf_{0.25}NiCu_{0.075}Sn$, (e) VFeSb, (f) $V_{0.8}Ti_{0.2}FeSb$ (g) $Nb_{0.8}Ti_{0.2}FeSb$. Panels (d) and (h) show the average $U_{iso}(T)$ for the XNiSn and X'FeSb samples, respectively. The solid lines are Debye fits as described in the text.

sensitivity to X-site composition is reflected in α_{av} which is 10.3×10^{-6} K^{-1} for VFeSb, 11.2×10^{-6} K^{-1} for $V_{0.8}Ti_{0.2}FeSb$, whilst $Nb_{0.8}Ti_{0.2}FeSb$ has a lower $\alpha_{av} = 8.9 \times 10^{-6}$ K^{-1} (table 1). The latter is in very good agreement with the reported $\alpha_{av} = 9.0(2) \times 10^{-6}$ K^{-1} for unsubstituted NbFeSb [36].

3.3.2. Atomic displacement parameters

The $U_{iso}(T)$ for the $XNiCu_ySn$ samples have similar magnitude except for the $Ti_{0.5}Zr_{0.25}Hf_{0.25}$ site (figures 4(a)–(c)), which has a slightly lower mean squared displacement, perhaps reflecting the segregated

Table 1. Overview of parameters used to fit $U_{iso}(T)$ and $a_{HH}(T)$ as described in the text of the manuscript. This includes the Debye temperatures for the individual atomic sites ($\theta_{D,i}$), the average value (θ_D) and the static disorder parameter (σ^2). The a_0 and b fit parameters are used to describe $a_{HH}(T)$. α_{av} is the average thermal expansion coefficient between 400 K and 848 K. The final columns show the calculated Debye velocity of sound (v_s), the 350 K lattice thermal conductivity ($\kappa_{lat,\,350\,K}$) and the calculated phonon mean free path (l_{MFP}). The κ_{lat} data for the XNiSn samples are from [45, 46].

	$\theta_{D,i}$ (K)/σ^2 ($\times10^{-2}$ Å^2)				a_0	b	α_{av}	$v_{s,}$	$\kappa_{lat,\,350\,K}$	l_{MFP}
Composition	X	Y	Z	Average	(Å)	($\times10^{-6}$)	($\times10^{-6}$ K^{-1})	(m s^{-1})	(W m^{-1} K^{-1})	($\times10^{-9}$ m)
TiNiSn	425(2)	381(2)	271(2)	339(2)	5.9211(1)	2.42	10.1	2947(40)	5.8	2.45(4)
	0	0	0	0						
$TiNiCu_{0.1}Sn$	403(2)	368(2)	259(2)	324(2)	5.9372(1)	2.49	10.4	2792(51)	4.2	1.86(3)
	0	0	0	0						
$Ti_{0.5}Zr_{0.25}Hf_{0.25}NiCu_{0.075}Sn$	323(2)	369(2)	265(2)	306(2)	5.9684(1)	2.36	9.8	2669(44)	2.6	1.24(3)
	0	0.029(5)	0.075(5)	0.012(5)						
VFeSb	434(2)	406(2)	271(2)	348(2)	5.8142(1)	2.44	10.3	2953(42)	5.6	2.22(3)
	0	0	0	0						
$V_{0.8}Ti_{0.2}FeSb$	419(2)	384(2)	258(2)	331(2)	HH1–5.8441(1)	HH1–2.66	11.2	2833(43)	5.3	2.24(3)
	0	0	0.054(5)	0.014(5)	HH2–5.8208(1)	HH2–2.50	10.6			
$Nb_{0.8}Ti_{0.2}FeSb$	356(2)	414(2)	290(2)	340(2)	5.9423(1)	2.14	8.9	2978(44)	7.4	3.16(5)
	0	0	0	0						

nature of the X-metals. The similar $U_{iso}(T)$ reflects the highly connected nature of the HH structure. The θ_{Di} for the individual sites and the average θ_D obtained from the simultaneous fit of the average $U_{iso}(T)$ and $a(T)$ are given in table 1. This reveals a modest reduction from $\theta_D = 339(2)$ K (X = Ti, y = 0) to $\theta_D = 324(2)$ K (X = Ti, y = 0.1) to $\theta_D = 306(2)$ K (X = $Ti_{0.5}Zr_{0.25}Hf_{0.25}$; y = 0.075), reflecting changes in bond strength and average atomic mass discussed below. Static disorder ($\sigma^2 > 0$) is only observed for the phase segregated $Ti_{0.5}Zr_{0.25}Hf_{0.25}NiCu_{0.1}Sn$ composition, and interestingly affects the Sn-site strongest, whilst the X-site itself shows no residual disorder. The TiNiSn and $TiNiCu_{0.075}Sn$ samples have $\sigma^2 = 0$ for all sites, indicating that incorporation of interstitial Ni/Cu does not lead to large amounts of residual disorder. The $U_{iso}(T)$ for the X'FeSb samples are also comparable (figures 4(e)–(g)), again evidencing the connected nature of the crystal structure. The individual θ_{Di} and the average θ_D are given in table 1. This reveals similar $\theta_D = 348(2)$ K (X' = V), $\theta_D = 331(2)$ K (X' = $V_{0.8}Ti_{0.2}$) and $\theta_D = 341(2)$ K (X' = $Nb_{0.8}Ti_{0.2}$). This contrasts with the XNiSn samples, where a decreasing trend was observed upon introduction of Cu interstitials and alloying with heavier elements on the X-site. The two-phase $V_{0.8}Ti_{0.2}FeSb$ sample is the only composition that shows significant residual disorder, again largely affecting the main group (Sb) sublattice (table 1). By contrast, $Nb_{0.8}Ti_{0.2}FeSb$ is single phase with good statistical mixing of Nb and Ti and has $\sigma^2 = 0$ for all sites (figure S5, table 1). This suggests that the observation of static residual disorder reflects poor atomic mixing on lattice sites and is linked to phase segregation.

Force constants: θ_D is proportional to the highest (cut-off) frequency (ω_D) in the Debye model, $k_B\theta_D = \hbar\omega_D$. Hence, $\theta_D \propto \sqrt{k/m}$ where k is the bond force constant and m the mass of the oscillator. The similar $\theta_D \sim 340$ K for the X'FeSb samples, reveals similar k for VFeSb and $V_{0.8}Ti_{0.2}FeSb$. By contrast, $Nb_{0.8}Ti_{0.2}FeSb$ with its larger average m, has an increased k to maintain a similar θ_D. The presence of a more rigid crystal structure is consistent with the reduced $\alpha(T)$ (figure 3(f)). The lower $\theta_D = 305$ K for $Ti_{0.5}Zr_{0.25}Hf_{0.25}NiCu_{0.1}Sn$ (compared to 340 K for TiNiSn) is almost completely explained by the 17% increase in average m. This suggests that the XNiSn compositions have similar k values, which is evident in the similar $\alpha(T)$ in figure 3(c). Phonon calculations support this conclusion with the changes in band dispersion in the XNiSn (Ti, Zr, Hf) system largely explained by increasing average mass [65]. The n- and p-type samples therefore present an intriguing difference; for XNiSn the k are similar, independent of X-site composition and notably also of interstitial metals, whereas the X-metal has a strong influence on k for the X'FeSb compositions.

The trends of θ_{Di} for the individual atomic sites is summarised in figure 5. This shows a plot of θ_{Di} ($\propto 1/m$) versus $\theta_{Di}\sqrt{m}$ ($\propto k$), which affords a visual way to separate the impact of increasing m and k. This analysis reveals clear trends, where sites with similar m are grouped together on diagonal lines. For example, the X-site elements Ti and V fall on a straight line with V on average further towards the right, indicating a larger k. Similar trends are observed for Fe/Ni on the Y site and Sn/Sb on the Z-site, with Fe and Sb typically appearing further towards the right. As expected, the θ_{Di} for NbFeSb extend out furthest towards the right, signalling a large k for all sites in the crystal structure.

Velocity of sound: The θ_D values can be used to obtain the velocity of sound using: $v_s = \theta_D (k_B/\hbar) \left(6\pi^2 n\right)^{-(1/3)}$, where n is the number density of atoms. The calculated v_s are given in table 1 and decrease from 2950 m s^{-1} (X = Ti; y = 0) to 2670 m s^{-1} (X = $Ti_{0.5}Zr_{0.25}Hf_{0.25}$; y = 0.075) and are similar for the X'FeSb samples with an average value $v_s = 2920(80)$ m s^{-1}. As expected, these trends directly follow the trends in θ_D. Compared to direct ultrasound measurements, the v_s values from the Debye model are somewhat suppressed. Table S3 gives an overview of reported longitudinal (v_L) and transverse (v_T) sound velocities, their average (v_m) and the calculated θ_D (using v_m) for a range of HH compounds. Compared to these data, the θ_D and v_s values obtained from fitting $U_{iso}(T)$ and $a(T)$ are ~15% reduced. For example, for TiNiSn and $Nb_{0.8}Ti_{0.2}FeSb$, we find $\theta_D = 340(2)$ K, whilst the value from ultrasound measurements is ~390 K. This discrepancy is larger than expected from the uncertainty in temperature and sample absorption. Our earlier neutron powder diffraction study, where sample absorption is much reduced yielded $\theta_D = 367(2)$ K for TiNiSn and $\theta_D = 317(2)$ K for $Ti_{0.5}Hf_{0.5}NiSn$ [41].

3.3.3. Thermal conductivity

Within the kinematic approximation $\kappa_{lat} = (1/3) C_v v_s l_{MFP}$, where $C_v = 3nk_B$ is the constant volume heat capacity ($T > \theta_D$) and l_{MFP} the phonon mean-free path. This equation ignores the frequency dependence of the vibrational spectrum and of the different phonon scattering mechanisms, e.g. point defects, boundary and Umklapp scattering, that limit l_{MFP} [60]. Nevertheless, this first approximation is useful for comparing general trends. The calculated l_{MFP} decrease from 3.2 nm for $Nb_{0.8}Ti_{0.2}FeSb$ to 2.2 nm for $VFe_{1.06}Sb$ and $V_{0.8}Ti_{0.2}Fe_{1.04}Sb$, reflecting the lower κ_{lat} for the VFeSb samples, since v_s does not change substantially (table 1). The l_{MFP} for the $XNiCu_ySn$ samples decreases from 2.5 nm ($TiNi_{0.04}Sn$) to 1.9 nm ($TiNiCu_{0.09}Sn$) to 1.2 nm ($Ti_{0.5}Zr_{0.25}Hf_{0.25}NiCu_{0.05}Sn$) as the concentration of interstitials and X-site alloying increases (table 1). TiNiSn without Ni interstitials has $l_{MFP} = 5$ nm ($\kappa_{lat} \sim 12$ W m^{-1} K^{-1} at 350 K) [44], whilst VFeSb

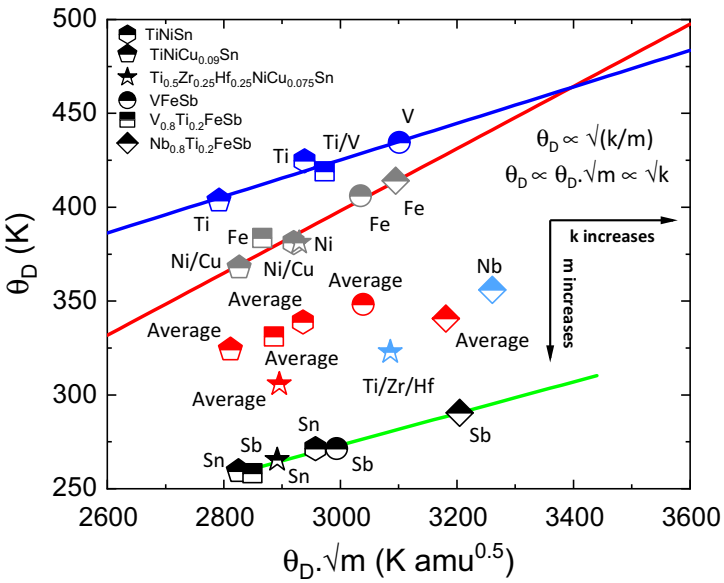

Figure 5. Phase field of θ_D versus of $\theta_D\sqrt{m}$ enabling separation of the impact of atomic mass and force constant on the Debye temperature for the studied HH materials.

with a regular $\kappa_{lat}(T)$ discussed above has $l_{MFP} = 4.4$ nm [50]. Both TiNiSn and VFeSb therefore show a ~50% reduction in l_{MFP} when 4%–6% Ni/Cu/Fe interstitials are introduced, demonstrating a similar impact in both materials systems. The X-site substitutions are also a significant contributor: for XNiSn, alloying with heavy elements (Zr/Hf) leads to a substantial reduction to $l_{MFP} = 1.2$ nm. The identical l_{MFP} for $VFe_{1.06}Sb$ and $V_{0.8}Ti_{0.2}Fe_{1.04}Sb$ suggests that Ti substitution contributes significantly towards reducing l_{MFP}, despite the similar mass and size of V/Ti. Unsubstituted NbFeSb has $l_{MFP} = 7$ nm ($\kappa_{lat} \sim 17$ W m^{-1} K^{-1} at 350 K) [12], which is reduced to 3.2 nm upon introduction of 20% Ti, confirming the strong impact of X-site disorder. We note that other phonon scattering contributions have been invoked for NbFeSb, including electron-phonon scattering [12], and recently scattering resulting from lamellar boundary interfaces [66].

4. Discussion

The simultaneous fitting of lattice and atomic displacement parameters has not been widely explored but affords new insight into the lattice dynamics of the HH alloys. In terms of the thermal expansion, the most striking result is the reduced $\alpha(T)$ for $Nb_{0.8}Ti_{0.2}FeSb$ compared to VFeSb. Our analysis shows that this is caused by a larger average bond force constant, i.e. a more rigid lattice structure. This is consistent with literature bulk modulus (B) data. Table S3 lists the B values calculated from velocity of sound measurements for a range of HH alloys. For XNiSn: $B \sim 125$ GPa; for XCoSb: $B \sim 135$ GPa, whilst a larger $B \sim 155$ GPa is found for NbFeSb. This increased B value is consistent with the lower $\alpha(T)$ for $Nb_{0.8}Ti_{0.2}FeSb$ found here from diffraction data. Amongst the HH alloys, NbFeSb therefore appears to be somewhat of an outlier with a large bulk modulus (B) and low thermal expansion (α).

For device applications, matching VFeSb with XNiSn is preferable because of the similar $\alpha(T)$. However, in terms of TE performance, much better performance is observed in NbFeSb. This may be related to the absence of interstitial metals, which reduce charge carrier mobilities in the better studied XNiSn system [41, 42], and cause the early onset of bipolar transport. On the other hand, the Fe interstitials are effective at reducing κ_{lat}, so further work exploring the balance between a low κ_{lat}, reducing performance degrading κ_{bi} and optimising S^2/ρ is warranted. The samples reported here can be improved further through process optimisation. In particular, for the VFeSb based samples, $\rho(T)$ needs to be reduced, whilst for NbFeSb, the degradation of the high-temperature $S(T)$ needs to be addressed. Both require the sample quality to be improved, including elimination of impurity phases and of porosity in the hot-pressed ingots.

To conclude, this synchrotron x-ray diffraction study provides new insight into the thermal properties of TiNiSn- and VFeSb-based HH alloys. In particular, VFeSb and TiNiSn are well matched in terms of thermal expansion and are both characterised by interstitial metals. Control of the Fe interstitials may significantly enhance the performance of p-type VFeSb. Amongst the highly studied HH alloys, NbFeSb is characterised by a large bulk modulus and low thermal expansion coefficient.

Data availability statement

The data that support the findings of this study are openly available at the following URL/DOI: https://doi.org/10.17861/4ca02b77-2585-4414-8ad4-1f4611f8e4cc [67].

Acknowledgments

J-W G B and S R P acknowledge the EPSRC for supporting the research on half-Heusler thermoelectrics (EP/N01717X/1). The STFC is acknowledged for allocation of synchrotron x-ray powder diffraction beamtime at the Diamond Light Source (EE17825).

ORCID iD

Jan-Willem G Bos https://orcid.org/0000-0003-3947-2024

References

[1] Rowe D M 2012 *Thermoelectrics and Its Energy Harvesting* (Boca Raton, FL: CRC Press)
[2] Liu W S, Jie Q, Kim H S and Ren Z F 2015 *Acta Mater.* **87** 357–76
[3] Bos J W G and Downie R A 2014 *J. Phys.: Condens. Matter* **26** 433201
[4] Zhu T J, Fu C G, Xie H H, Liu Y T and Zhao X B 2015 *Adv. Energy Mater.* **5** 1500588
[5] Huang L H, Zhang Q Y, Yuan B, Lai X, Yan X and Ren Z F 2016 Mater *Res. Bull.* **76** 107–12
[6] Yu J J, Xia K Y, Zhao X B and Zhu T J 2018 *J. Phys. D: Appl. Phys.* **51** 113001
[7] Poon S J 2019 *J. Phys. D: Appl. Phys.* **52** 493001
[8] Bos J-W G 2021 *Thermoelectric Energy Conversion* ed R Funahashi (Duxford: Woodhead Publishing) pp 125–42
[9] Graf T, Felser C and Parkin S S P 2011 *Prog. Solid State Chem.* **39** 1–50
[10] Chen S and Ren Z 2013 *Mater. Today* **16** 387–95
[11] Joshi G *et al* 2014 *Energy Environ. Sci.* **7** 4070–6
[12] He R *et al* 2016 *Proc. Natl Acad. Sci. USA* **113** 13576–81
[13] Zhu H T *et al* 2018 *Nat. Commun.* **9** 2497
[14] Zhu H T *et al* 2019 *Nat. Commun.* **10** 270
[15] Hermet P, Ayral R M, Theron E, Yot P G, Salles F, Tillard M and Jund P 2014 *J. Phys. Chem.* C **118** 22405–11
[16] Petersen A, Bhattacharya S, Tritt T M and Poon S J 2015 *J. Appl. Phys.* **117** 035706
[17] Pang H J, Chen L C, Cao Z Y, Yu H, Fu C G, Zhu T J, Goncharov A F and Chen X J 2018 *J. Appl. Phys.* **124** 195107
[18] Yan X A *et al* 2011 *Nano Lett.* **11** 556–60
[19] Schwall M and Balke B 2013 *Phys. Chem. Chem. Phys.* **15** 1868–72
[20] Chen L, Gao S, Zeng X, Dehkordi A M, Tritt T M and Poon S J 2015 *Appl. Phys. Lett.* **107** 041902
[21] Rausch E, Balke B, Stahlhofen J M, Ouardi S, Burkhardt U and Felser C 2015 *J. Mater. Chem.* C **3** 10409–14
[22] Liu Y T, Fu C G, Xia K Y, Yu J J, Zhao X B, Pan H G, Felser C and Zhu T J 2018 *Adv. Mater.* **30** 1800881
[23] Gurth M, Rogl G, Romaka V V, Grytsiv A, Bauer E and Rogl P 2016 *Acta Mater.* **104** 210–22
[24] Rogl G, Sauerschnig P, Rykavets Z, Romaka V V, Heinrich P, Hinterleitner B, Grytsiv A, Bauer E and Rogl P 2017 *Acta Mater.* **131** 336–48
[25] Fu C, Bai S, Liu Y, Tang Y, Chen L, Zhao X and Zhu T 2015 *Nat. Commun.* **6** 8144
[26] Fu C G, Zhu T J, Liu Y T, Xie H H and Zhao X B 2015 *Energy Environ. Sci.* **8** 216–20
[27] Xia K, Liu Y, Anand S, Snyder G J, Xin J, Yu J, Zhao X and Zhu T 2018 *Adv. Funct. Mater.* **28** 1705845
[28] Ferluccio D A, Smith R I, Buckman J and Bos J-W G 2018 *Phys. Chem. Chem. Phys.* **20** 3979–87
[29] Ferluccio D A, Halpin J E, MacIntosh K L, Quinn R J, Don E, Smith R I, MacLaren D A and Bos J-W G 2019 *J. Mater. Chem.* C **7** 6539
[30] Bartholomé K, Balke B, Zuckermann D, Köhne M, Müller M, Tarantik K and König J 2014 *J. Electron. Mater.* **43** 1775–81
[31] Zhang Y L, Cleary M, Wang X W, Kempf N, Schoensee L, Yang J, Joshi G and Meda L 2015 *Energy Convers. Manage.* **105** 946–50
[32] Black D, Schoensee L, Richardson J, Vleisides T, Kempf N, Wang D Z, Ren Z F and Zhang Y L 2018 *ACS Appl. Energy Mater.* **1** 5986–92
[33] Xing Y F *et al* 2019 *Energy Environ. Sci.* **12** 3390–9
[34] Yu J J *et al* 2020 *Adv. Energy Mater.* **10** 2000888
[35] Rogl G *et al* 2016 *Acta Mater.* **107** 178–95
[36] Silpawilawan W, Kurosaki K, Ohishi Y, Muta H and Yamanaka S 2017 *J. Mater. Chem.* C **5** 6677–81
[37] Hazama H, Matsubara M, Asahi R and Takeuchi T 2011 *J. Appl. Phys.* **110** 063710
[38] Birkel C S, Douglas J E, Lettiere B R, Seward G, Verma N, Zhang Y C, Pollock T M, Seshadri R and Stucky G D 2013 *Phys. Chem. Chem. Phys.* **15** 6990–7
[39] Downie R A, MacLaren D A, Smith R I and Bos J W G 2013 *Chem. Commun.* **49** 4184–6
[40] Douglas J E, Birkel C S, Verma N, Miller V M, Miao M S, Stucky G D, Pollock T M and Seshadri R 2014 *J. Appl. Phys.* **115** 043720
[41] Downie R A, Barczak S A, Smith R I and Bos J W G 2015 *J. Mater. Chem.* C **3** 10534–42
[42] Downie R A, Smith R I, MacLaren D A and Bos J W G 2015 *Chem. Mater.* **27** 2449–59
[43] Tang Y L, Li X S, Martin L H J, Reyes E C, Ivas T, Leinenbach C, Anand S, Peters M, Snyder G J and Battaglia C 2018 *Energy Environ. Sci.* **11** 311–20
[44] Barczak S A, Buckman J, Smith R I, Baker A R, Don E, Forbes I and Bos J-W G 2018 *Materials* **11** 536
[45] Barczak S A, Halpin J E, Buckman J, Decourt R, Pollet M, Smith R I, MacLaren D A and Bos J-W G 2018 *ACS Appl. Mater. Interfaces* **10** 4786–93
[46] Barczak S A *et al* 2019 *J. Mater. Chem.* A **7** 27124–34

[47] Young D P, Khalifah P, Cava R J and Ramirez A P 2000 *J. Appl. Phys.* **87** 317–21
[48] Jodin L, Tobola J, Pecheur P, Scherrer H and Kaprzyk S 2004 *Phys. Rev.* B **70** 184207
[49] Guo S P, Yang K S, Zeng Z and Zhang Y S 2018 *Phys. Chem. Chem. Phys.* **20** 14441–9
[50] Fu C G, Xie H H, Liu Y T, Zhu T J, Xie J and Zhao X B 2013 *Intermetallics* **32** 39–43
[51] Huang Y, Hayashi K and Miyazaki Y 2020 *Chem. Mater.* **32** 5173–81
[52] Thompson S, Parker J, Potter J, Hill T, Birt A, Cobb T, Yuan F and Tang C 2009 *Rev. Sci. Instrum.* **80** 075107
[53] Pearson W B 1958 *A Handbook of Lattice Spacing and Structures of Metals and Alloys* (Oxford: Pergamon Press)
[54] Larson A C and Von Dreele R B 2000 Los Alamos national laboratory report LAUR, 86–748
[55] Toby B H 2001 *J. Appl. Crystallogr.* **34** 210–3
[56] Tavassoli A, Failamani F, Grytsiv A, Rogl G, Heinrich P, Muller H, Bauer E, Zehetbauer M and Rogl P 2017 *Acta Mater.* **135** 263–76
[57] Hobbis D, Hermann R P, Wang H, Parker D S, Pandey T, Martin J, Page K and Nolas G S 2019 *Inorg. Chem.* **58** 1826–33
[58] Kim H S, Gibbs Z M, Tang Y L, Wang H and Snyder G J 2015 *APL Mater.* **3** 041506
[59] Glassbrenner C J and Slack G A 1964 *Phys. Rev.* **134** 1058
[60] Toberer E S, Zevalkink A and Snyder G J 2011 *J. Mater. Chem.* **21** 15843–52
[61] Naydenov G A, Hasnip P J, Lazarov V K and Probert M I J 2019 *J. Phys. Mater.* **2** 035002
[62] Popuri S R, Pollet M, Decourt R, Viciu M L and Bos J W G 2017 *Appl. Phys. Lett.* **110** 253903
[63] Popuri S R, Decourt R, McNulty J A, Pollet M, Fortes A D, Morrison F D, Senn M S and Bos J W G 2019 *J. Phys. Chem.* C **123** 5198–208
[64] Sales B C, Chakoumakos B C, Mandrus D and Sharp J W 1999 *J. Solid State Chem.* **146** 528–32
[65] Eliassen S N H, Katre A, Madsen G K H, Persson C, Lovvik O M and Berland K 2017 *Phys. Rev.* B **95** 045202
[66] Jeong H, Kihoi S K, Kahiu J N, Kim H, Ryu J, Lee K H, Yi S and Lee H S 2021 *J. Eur. Ceram. Soc.* **41** 4175–81
[67] Ferluccio D A, Kennedy B F, Barczak S A, Popuri S R, Murray C, Pollet M and Bos J-W G Dataset for Thermal properties of TiNiSn and VFeSb half-Heusler thermoelectrics from synchrotron X ray powder diffraction (available at: https://doi.org/10.17861/4ca02b77-2585-4414-8ad4-1f4611f8e4cc)